

## **Appendix F: Evolution of Porosity, Permeability, Ultrasonic Velocity and Pore Structure in Mudstone upon Fluid Injection**

### **Introduction**

Anthropogenic activities such as wastewater disposal, hydraulic fracturing and carbon sequestration involve injection of large fluid volumes into mudstone beds in the subsurface. This fluid injection results in the dilation of the mudstone pore structure through different mechanisms such as isotropic dilation, microfracturing and macrofracture propagation [Backeberg et al., 2017; Mayerhofer et al., 2006; Slatt and O'Brien, 2011]. Experimental studies record an increase in vertical mudstone permeability of an order of magnitude upon fluid injection volumes corresponding to 2-5% of sample porosity [Dong et al., 2010; Backeberg et al., 2017]. To understand the observed increase in mudstone permeability upon fluid injection, several models employ the effective stress law [Terzaghi, 1951],

$$\sigma_{eff} = \sigma_v - P_p \quad , \quad (A6.1)$$

where  $\sigma_v$  is the confining pressure on rock (Pa) and  $P_p$  is the pore pressure of fluids (Pa). Fluid injection in mudstone results in an increase in  $P_p$  and a subsequent decline in  $\sigma_v$ , a process known as unloading [Walsh, 1981].

Several models have been proposed to understand the dependence of mudstone permeability on effective stress upon fracture growth during fluid injection. Experimental observations from Backeberg et al. [2017] derive indicate a log-linear relationship between vertical permeability and effective stress in mudstones during fluid injection. Carey et al. [2015] utilize X-ray tomography and finite-discrete element modeling to propose a linear relationship between vertical permeability and effective stress in Utica Shale. Field-scale analysis of shale permeability indicate a log-linear relationship with effective stress during fluid injection [Chen et al., 2015]. While several studies have quantified the changes in fracture permeability with effective stress during fluid injection, the mechanistic response of the mudstone pore structure to injection remain unconstrained. During the backflow phase of hydraulic fracturing, only 20-30% of the injected water is recovered [Nicot and Scanlon, 2012], indicating that the majority of injected fluid resides within the host mudstone matrix [O'Malley et al., 2016]. Goodfellow et al. [2015], show that the growth of hydraulic fractures accounts for 18% to 94% of injection energy, indicating that a large fraction of injected fluid is not stored within the induced fractures. This potentially matrix held water can result in productivity and environmental concerns. The injected water can reside in small pores within the matrix and separate hydrocarbon from the fracture network [Dutta et al., 2012]. Additionally, the injected water may mix with salt and metals in the mudstone system and migrate to the groundwater leading to contamination of drinking water resources [Gallegos et al., 2015]. Thus, it is important to quantify the mechanistic response of the

mudstone pore structure to injected fluid to quantify mechanisms of accommodation of injected fluid.

We conduct an experimental investigation into the evolution of the porosity, permeability and acoustic velocity in a natural mudstone sample during fluid injection. We combine the measured petrophysical characteristics with volumetric changes of the sample during fluid injection to infer pore structure changes during fluid injection. We employ the petrophysical parameters to understand the partitioning of injected fluid between elastic and inelastic deformation within the mudstone sample. Our results can improve constraints upon the response of mudstones to fluid injection during anthropogenic activities such as wastewater disposal, hydraulic fracturing and carbon sequestration.

## Methods

I measure the porosity ( $\phi$ ), vertical permeability ( $k_v$ ) and acoustic P-wave velocity ( $V_p$ ), acoustic S-wave velocity ( $V_s$ ) during step-wise consolidation and fluid injection in mudstone sample 3H-4 from IODP Expedition 308. Sample 3H-4 was cored perpendicular to bedding in Hole 1324B at an insitu depth of 18.4 mbsf, corresponding to a preconsolidation stress of 416 kPa [Sawyer et al., 2006]. Sample 3H-4 has an initial porosity of 0.65 and consists of 1% sand, 36% silt and 62% clay by grain size [Sawyer et

al., 2006]. The sample has an initial radius ( $r_i$ ) of 0.0127 m and a height ( $h_i$ ) of 0.033 m, corresponding to an initial sample volume ( $V_i$ ) of  $1.66 \times 10^{-5} \text{ m}^3$ .

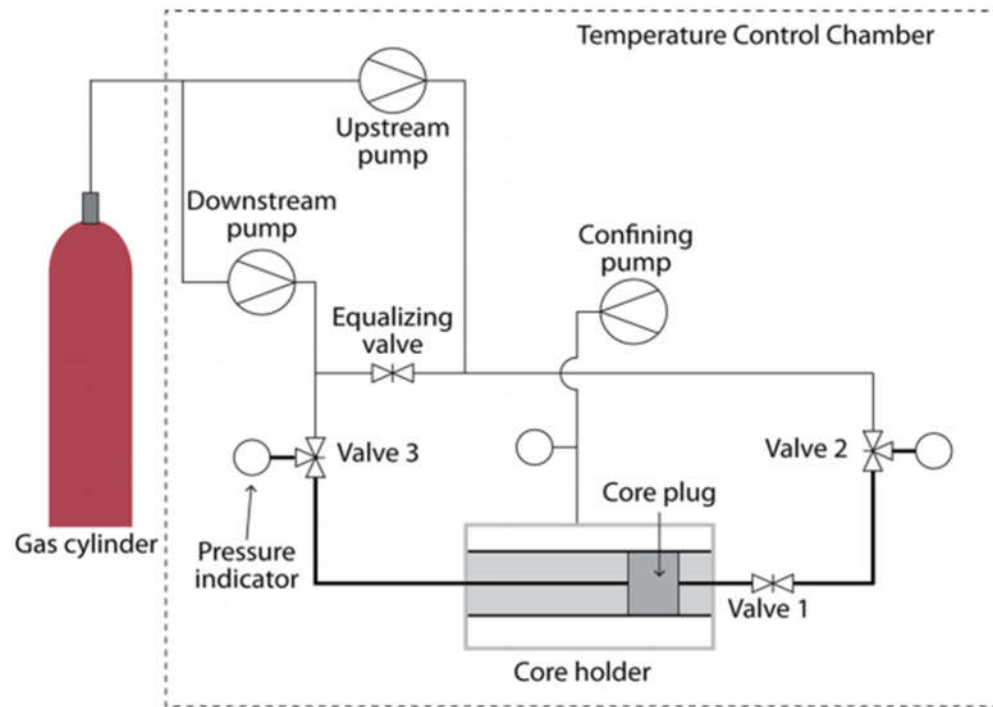


**Figure A6.1 - Schematic diagram for the experimental setup used in our experiment [from Bhandari et al., 2015].**

The core plug is enclosed in a Viton sleeve and mounted in a National Instruments pressure cell held within a temperature-controlled chamber [Fig A6.1]. The setup consists of two pore pressure pumps, one confining pressure pump, a coreholder, plumbing lines with valve fittings, temperature control and data acquisition systems. The temperature of the setup is maintained at 30° C during the biaxial test. We use two Quizix



Laboratory ultrasonic measurements were performed using the National Instruments pressure vessel with three 500 kHz central frequency piezoelectric transducers embedded in the endcaps [Fig A6.2]. Sample length was monitored for the duration of the experiment using a linear potentiometer displacement transducer attached to the axial ram [Fig A6.2].

### **Stress Pathway for Fluid Injection Experiment**

We conduct two stages of fluid injection in our experiment to analyze the elastic and inelastic response of mudstone to fluid injection. In the first stage of loading, the confining pressure on rock is increased from 0 psi to 943 psi in five steps [Fig A6.3], Simultaneously, pore pressure in the sample is increased from 0 psi to 379 psi in five steps, resulting in an increase in effective stress from 0 to 564 psi [Fig A3.3]. In the first stage of unloading, the pore pressure is increased from 379 psi to 602 in two steps, resulting in a decline in effective stress from 564 psi to 341 psi [Fig A6.3]. Pore pressure is reduced from 602 psi to 377 psi to begin the second loading phase. In the second stage of loading, the confining pressure on rock is increased from 943 psi to 1876 psi in two steps [Fig A6.3], Simultaneously, pore pressure in the sample is increased from 377 psi to 758 psi in two, resulting in an increase in effective stress from 562 psi to 1122 psi [Fig A6.3]. In the second stage of unloading, the pore pressure is increased from 753 psi to 1895 in seven steps, resulting in a decline in effective stress from 1122 psi to -20 psi [Fig A6.3]. We conduct vertical permeability ( $k_v$ ), p-wave velocity ( $V_p$ ), S-wave velocity ( $V_s$ ),

Axial Strain ( $\epsilon_a$ ) and radial strain ( $\epsilon_r$ ) measurements at each step of loading and unloading. All permeability and acoustic measurements are conducted at confining stress states higher than insitu overburden stress to avoid effects of preconsolidation on petrophysical signatures. Backpressure saturation was conducted for pore pressures ranging from 125 psi to 250 psi and saturation was established once stabilized B-values of 0.95 were attained [Skempton, 1954].

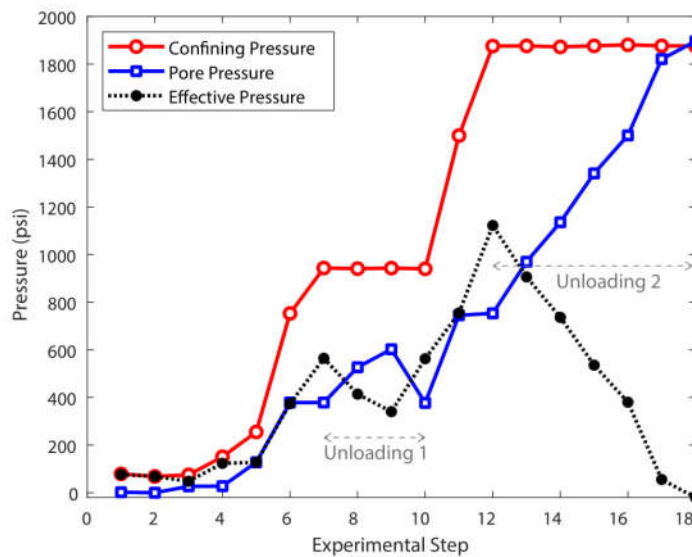


**Figure A6.3. - Evolution of Effective Pressure as a function of prescribed Confining Pressure and Pore Pressure pathways during two-stage unloading test on sample 3H-4.**

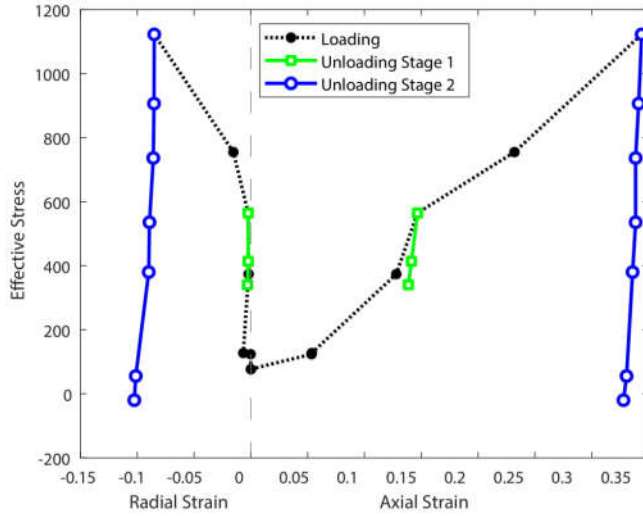


**Figure A6.4 - Evolution of axial Strain and radial Strain of sample 3H-4 during Loading, Unloading Stage 1 and Unloading Stage 2. Unloading Stage 1 is characterized by a decline in axial strain, whereas Unloading Stage 2 is characterized by a decline in both axial and radial strain.**

### Strain and Porosity Calculations

The total volume of sample at each step of loading and unloading ( $V$ ) is calculated using the volume of water injected or removed ( $\Delta V_{inj}$ ) as

$$V = V_i + \Delta V_{inj} \quad . \quad (A6.2)$$



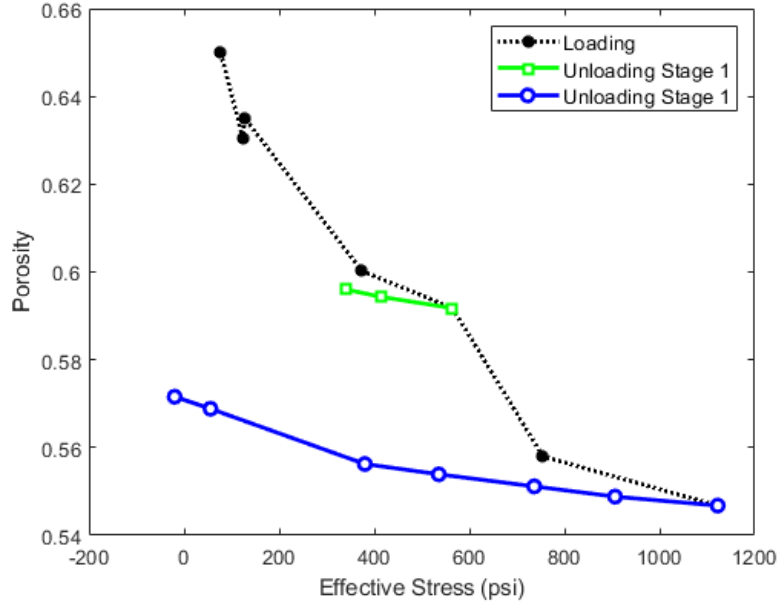


**Figure A6.5 - Evolution of porosity of sample 3H-4 during Loading, Unloading Stage 1 and Unloading Stage 2. Porosity rebound from 0.60 to 0.59 during Unloading Stage 1 indicates elastic dilation, whereas porosity increases from 0.55 to 0.57 during Unloading Stage 2 indicates fracture growth.**

At each step of loading and unloading, we calculate the height of the sample ( $h$ ) using the change height of sample ( $\Delta h$ ) recorded by the linear potentiometer displacement transducer as

$$h = h_i + \Delta h \quad . \quad (A6.3)$$

Axial Strain ( $\varepsilon_a$ ) at each step is calculated as

$$\varepsilon_a = h/h_i \quad . \quad (A6.4)$$

Similarly, we calculate the radius of the cylindrical sample ( $r$ ) and associated radial strain ( $\varepsilon_r$ ) at each step of loading and unloading as

$$r = \sqrt{V/\pi h} \quad , \quad (A6.5)$$

$$\varepsilon_r = r/r_i \quad . \quad (A6.6)$$

At each step of loading and unloading, we calculate the porosity ( $\phi$ ) of the sample as

$$\phi = (\phi_i * V_i) + \Delta V_{inj} \quad , \quad (A6.7)$$

where ( $\phi_i * V_i$ ) represents the initial pore volume of the sample at  $\phi=0.65$ . The evolution of  $\varepsilon_a$ ,  $\varepsilon_r$  and  $\phi$  provides us with a quantitative measure of change in pore structure of the mudstone sample [Fig A6.4; Fig A6.5].

### Calculation of Vertical Permeability

At each step of loading and unloading, we calculate vertical mudstone permeability by rearranging Darcy's Law as

$$k_v = \frac{\mu * q * h}{A \Delta P} \quad , \quad (A6.8)$$

where  $k_v$  is vertical permeability ( $\text{m}^2$ ),  $\mu$  is the viscosity of the fluid ( $\text{Pa.s}$ ),  $q_v$  is the vertical flux of fluid, and  $h$  is the height of the sample ( $\text{m}$ ), and  $\Delta P$  is the pressure differential is applied across the sample ( $\text{Pa}$ ). In our flow through permeability tests, we

use distilled water as the permeating fluid (dynamic viscosity,  $\mu = 8.9 \times 10^{-4}$  Pa·s) and maintain a constant pressure differential ( $\Delta P$ ) of 0.51 MPa across the mudstone sample. The evolution of vertical permeability ( $k_v$ ) provides a quantitative measure of evolving transport properties of mudstone upon fluid injection [Fig A6.6].

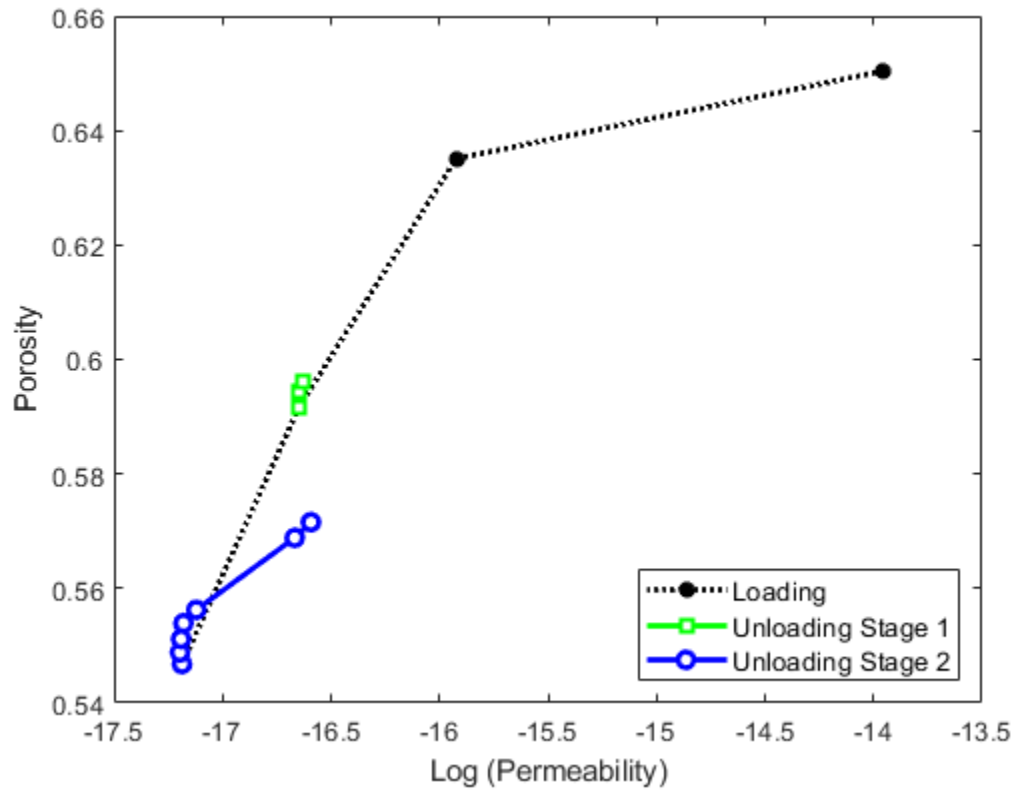


**Figure A6.6 - Evolution of vertical permeability ( $k_v$ ) of sample 3H-4 during Loading, Unloading Stage 1 and Unloading Stage 2.  $k_v$  triples in magnitude during Unloading Stage 1 indicates dilation of pore throats; the increase in  $k_v$  of over two orders of magnitude during Unloading Stage 2 indicates fracture growth.**

### Compressional ( $V_p$ ) and Shear Wave ( $V_s$ ) Velocity

Ultrasonic velocities ( $V_p$  and  $V_s$ ) exhibit an inverse relationship with effective stress rock [Bowers, 1995; Jeppson and Tobin, 2015]. In particular  $V_p$  and  $V_s$  are strong indicators of rock fracture, exhibiting a sharp decline upon fracture initiation in mudstones [Kuila et al., 2011; Dewhurst and Siggins, 2006]. At each step of unloading, we measure bedding-perpendicular ultrasonic velocities ( $V_p$  and  $V_s$ ) to infer accommodation mechanism for injected fluid, especially the onset of fluid injection induced fractures [Fig A6.7; Fig A6.8].

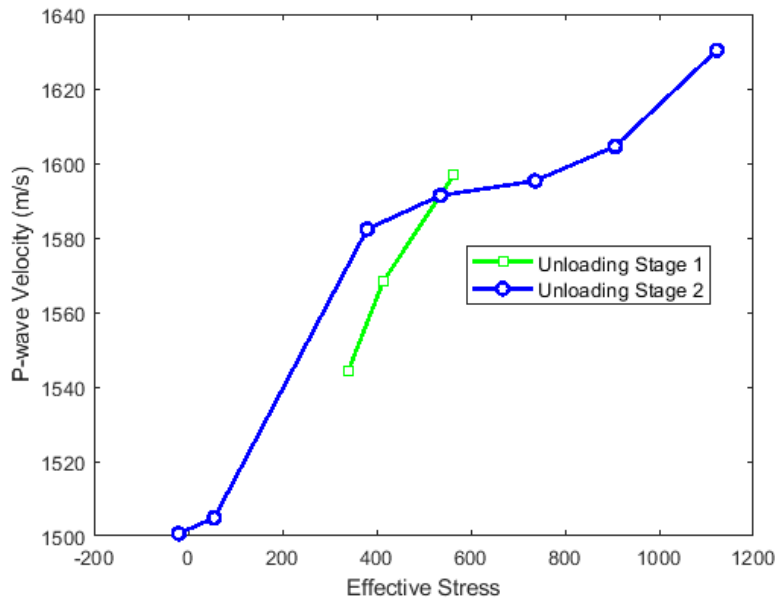


**Figure A6.7 -  $V_p$  measurements from sample 3H-4 exhibit an inverse relationship with effective pressure during Unloading Stage 1 and Unloading Stage 2.**

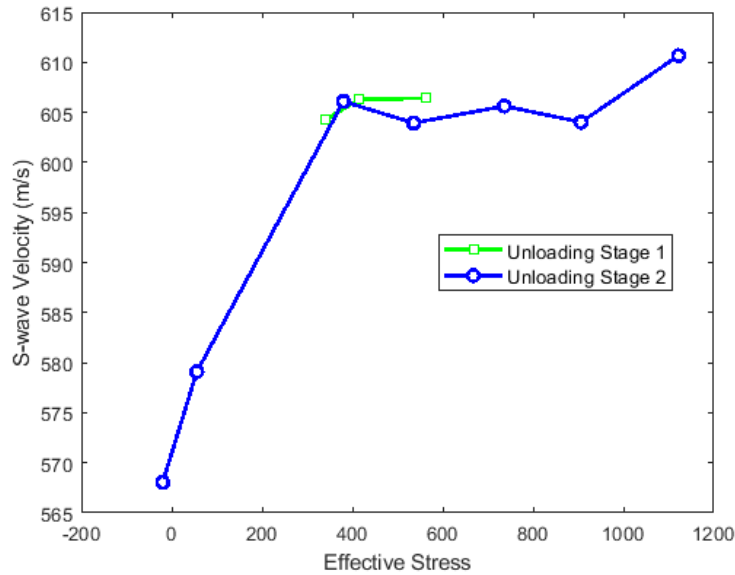


**Figure A6.8 -  $V_s$  measurements from sample 3H-4 exhibit an inverse relationship with effective pressure during Unloading Stage 1 and Unloading Stage 2.**

## Results

The first stage of loading corresponds to an increase in the effective stress on the sample from 0 to 564 psi in five steps [Fig A6.3]. We calculate an increase in axial strain ( $\epsilon_a$ ) from 0 to 0.147, indicating a decline in height of the sample [Fig A6.4].

Simultaneously, we calculate a decline in radial strain ( $\epsilon_r$ ) from 0 to  $-2.3 \times 10^{-3}$ , indicating an increase in radius of the sample [Fig A6.4]. We calculate a decline in porosity ( $\phi$ ) from 0.65 to 0.59 during the first stage of loading [Fig A6.5] and correlated decline in vertical permeability ( $k_v$ ) from  $1.11 \times 10^{-14} \text{ m}^2$  to  $2.26 \times 10^{-17} \text{ m}^2$  [Fig A6.6].

The first stage of unloading corresponds to a decline in the effective stress on the sample from 564 psi to 341 psi in two steps [Fig A6.3]. We calculate a decline in  $\varepsilon_a$  from 0.147 to 0.138, indicating an increase in height of the sample [Fig A6.4]. Simultaneously, we calculate a decline in  $\varepsilon_r$  from  $-2.3 \times 10^{-3}$  to  $-2.94 \times 10^{-3}$  indicating a small increase in the radius of the sample [Fig A6.4]. We calculate an increase in  $\phi$  from 0.59 to 0.60 during the first stage of unloading [Fig A6.5] and correlated increase in  $k_v$  from  $2.26 \times 10^{-17} \text{ m}^2$  to  $2.36 \times 10^{-17} \text{ m}^2$  [Fig A6.6]. Fluid injection during the first stage of unloading corresponds to a decline in compressional wave velocity ( $V_p$ ) from 1597 m/s to 1544 m/s [Fig A6.7], and a decline in shear wave velocity ( $V_s$ ) from 606 m/s to 604 m/s [Fig A6.8]. At the conclusion of the first stage of unloading, we reduce the pore pressure from 603 psi to 377 psi and calculate a decline in porosity from 0.60 to 0.59, indicating that fluid injection in this stage resulted in elastic dilation of pore spaces.

The second stage of loading corresponds to an increase in the effective stress from 943 psi to 1876 psi in two steps [Fig A6.3]. We calculate an increase in axial strain ( $\varepsilon_a$ ) from  $1.47 \times 10^{-1}$  to  $3.44 \times 10^{-1}$ , indicating a decline in height of the sample [Fig A6.4]. Simultaneously, we calculate a decline in radial strain ( $\varepsilon_r$ ) from  $-2.3 \times 10^{-3}$  to  $-8.5 \times 10^{-2}$ , indicating an increase in radius of the sample [Fig A6.4]. We calculate a decline in porosity ( $\phi$ ) from 0.59 to 0.54 during the second stage of loading [Fig A6.5] and correlated decline in vertical permeability ( $k_v$ ) from  $2.26 \times 10^{-17} \text{ m}^2$  to  $6.51 \times 10^{-18} \text{ m}^2$  [Fig A6.6].

The second stage of unloading corresponds to a decline in the effective stress on the sample from 1122 psi to -20 psi in six steps [Fig A6.3]. We calculate a decline in  $\varepsilon_a$  from  $3.44 \times 10^{-1}$  to  $3.28 \times 10^{-1}$ , indicating an increase in height of the sample [Fig A6.4]. Simultaneously, we calculate a decline in  $\varepsilon_r$  from  $-8.5 \times 10^{-2}$  to  $-1.02 \times 10^{-1}$  indicating a small increase in the radius of the sample [Fig A6.4]. We calculate an increase in  $\phi$  from 0.54 to 0.57 during the first stage of unloading [Fig A6.5] and correlated increase in  $k_v$  from  $6.51 \times 10^{-18} \text{ m}^2$  to  $2.56 \times 10^{-17} \text{ m}^2$  [Fig A6.6]. Fluid injection during the second stage of unloading corresponds to a decline in  $V_p$  from 1630 m/s to 1501 m/s, with a sharp decline as effective stress on rock approaches zero [Fig A6.7]. Similarly, we calculate a decline and a decline in  $V_s$  from 610 m/s to 568 m/s with a sharp decline as effective stress on rock approaches zero [Fig A6.8].

## Discussions

We develop a simplistic mudstone model to explain the mechanistic pore-scale response of the sample to loading and fluid injection. We build our mudstone models from cuboidal platelets arranged in bedding layers. Pore space between particles is defined by intrabed pores of a finite width ( $\varepsilon$ ) and by interbed pores, each of length and width ( $\lambda$ ) [Fig A6.9a]. Vertical permeability is derived from water flux ( $q_v$ ) perpendicular to bedding [Fig A6.9a]. We assume that the dimensions of clay platelets remain constant; compaction and fluid injection result in changes to the interbed and intrabed pores.

Compaction from equal axial and radial confining pressure results in a reduction in interbed and intrabed pore throats [Fig A6.9b]. The reduction in pore throat diameters during loading results in the measured increase in axial and decline in radial strain, indicating a decline in the volume of the sample [Fig A6.4]. The reduction in pore throat diameters during loading results in the decline in porosity of the sample [Fig A6.5] and vertical permeability [Fig A6.6].

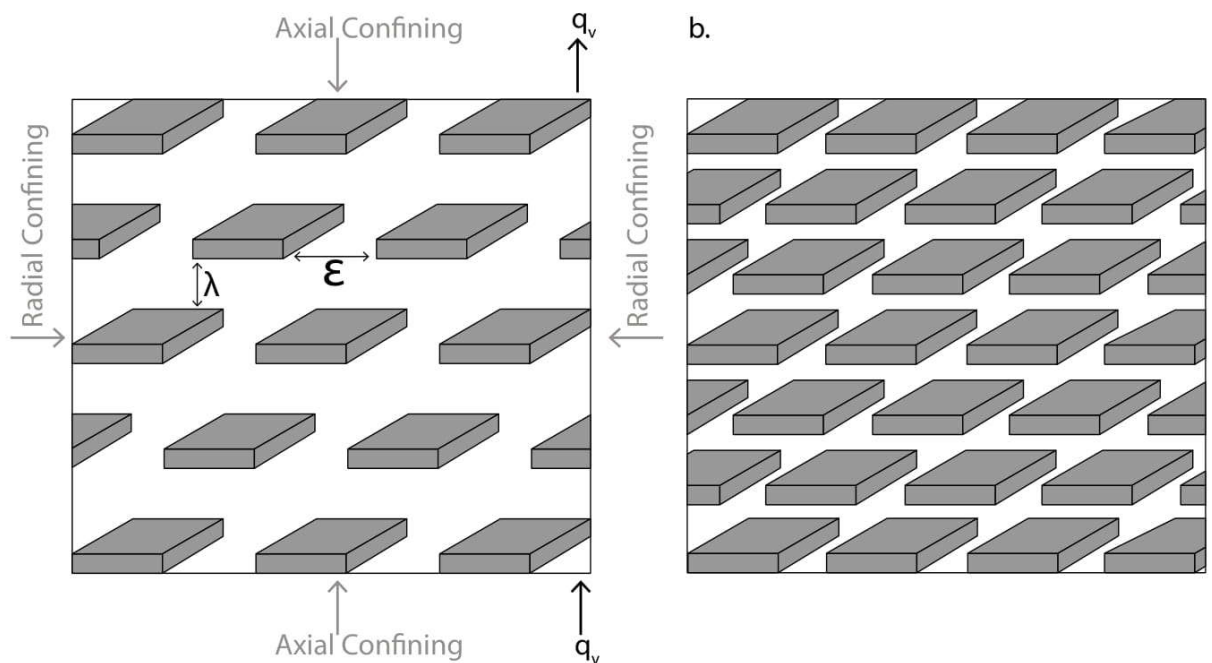


**Figure A6.9 - (a) Schematic of mudstone model consisting of clay platelets (grey cuboids) and intrabed ( $\epsilon$ ) and interbed ( $\lambda$ ) pore throat widths. Flux of fluid perpendicular to bedding direction ( $q_v$ ) is used to calculate the vertical permeability ( $k_v$ ). (b) Mudstone model after compaction by reduction in pore throat widths,  $\epsilon$  and  $\lambda$ .**



We inject  $1.5 \times 10^{-7} \text{ m}^3$  of fluid during Unloading Stage 1 resulting in an elastic increase in porosity from 0.59 to 0.60. The porosity of the sample exhibiting a linear relationship with effective stress of the form  $\phi = -1.87 \times 10^{-5} \sigma_{eff} + 0.6$ . The measurements of strain and porosity indicate that the injected fluid volume is predominantly accommodated by dilation of interbed pores [Fig A6.10a], resulting in a small increase in vertical permeability [Fig A6.6] and decline in ultrasonic velocities ( $V_p$  and  $V_s$ ) [Fig A6.7; Fig A6.8].

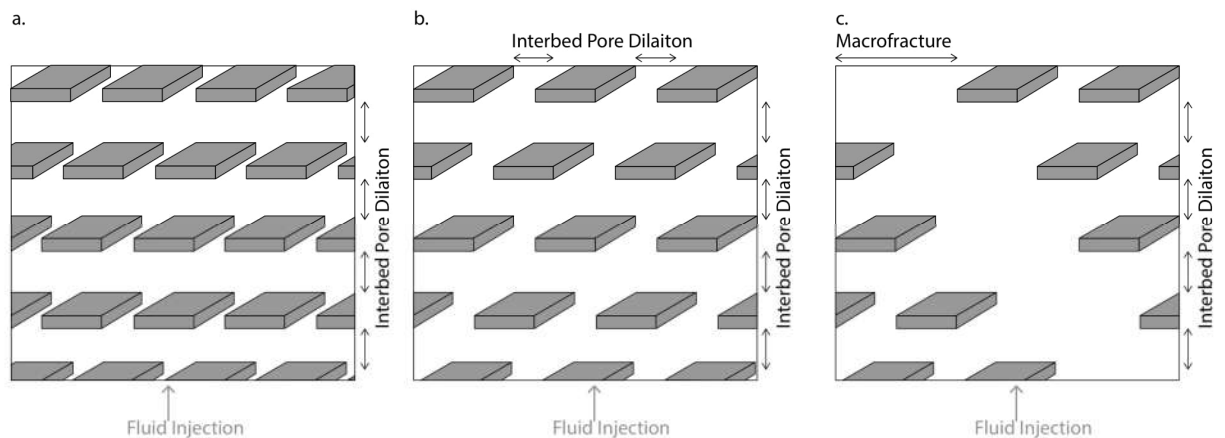


**Figure A6.10 - Schematic of (a) interbed pore dilation in mudstone sample during fluid injection in Unloading Stage 1; (b) interbed and interbed pore dilation in mudstone sample during fluid injection in Unloading Stage 2 upon pore pressure increase from 753 psi to 1500 psi; and (c) macrofracture growth in mudstone sample during fluid injection in Unloading Stage 2 upon pore pressure increase from 1500 to 1821 psi.**

Fluid injection during Unloading Stage 2 shows two characteristic phases - the first phase consists of five steps as pore pressure is increased from 753 psi to 1500 psi ,

the second phase consists of two steps as pore pressure is increased from 1500 to 1821 psi. During pore pressure increase from 753 psi to 1500 psi, we inject  $2.74 \times 10^{-7} \text{ m}^3$  of fluid into the sample, resulting in an increase in porosity from 0.54 to 0.57. The porosity of the sample exhibits a linear relationship with effective stress of the form  $\phi = -1.29 \times 10^{-5} \sigma_{eff} + 0.56$ . This is similar to the elastic dilation observed in Unloading Stage 1. The measurements of strain and porosity indicate that the injected fluid volume is accommodated by dilation of intrabed and interbed pores [Fig A6.10b], resulting in a small increase in vertical permeability [Fig A6.6] and decline in ultrasonic velocities ( $V_p$  and  $V_s$ ) [Fig A6.7; Fig A6.8].

During pore pressure increase from 1500 to 1821 psi, we inject  $4.6 \times 10^{-7} \text{ m}^3$  of fluid into the sample, resulting in an increase in porosity from  $\phi = -3.84 \times 10^{-5} \sigma_{eff} + 0.57$ . The increase in slope of the porosity-effective stress character is accompanied by 3.4 times increase in vertical permeability [Fig A6.6], and a sharp decline in  $V_p$  and  $V_s$  [Fig A6.7; Fig A6.8]. The sharp increase in porosity and permeability along with the decline in ultrasonic velocities suggests the development of a macrofracture through the sample [Fig A6.10c].

The total volume of injected fluid ( $V_{total}$ ) during Unloading Stage 2 is  $7.43 \times 10^{-7} \text{ m}^3$ . Based on our measurements of porosity, permeability and ultrasonic velocities that the volume of fluid injected during pore pressure increase from 753 psi to 1500 psi results in elastic deformation of the mudstone matrix ( $V_{matrix}$ ), whereas the volume of

fluid injected during pore pressure increase from 1500 to 1821 psi results in inelastic deformation from fracture growth ( $V_{fracture}$ ). We calculate values of 0.37 and 0.63 for values of  $V_{matrix}/V_{total}$  and  $V_{fracture}/V_{total}$  respectively. Our results show that approximately 37% of the injected fluid is accommodated in the mudstone matrix during fluid injection. The loss of injected fluid to the mudstone matrix, accommodated by dilation of pore spaces, can explain the poor recovery of fluids during the flowback phase of hydraulic fracturing [Nicot and Scanlon, 2012; O'Malley et al., 2016]. Additionally, our results indicate that 63% of the injected fluid and corresponding injection energy are partitioned into fracture formation. Our results support the results of Goodfellow et al. [2015], showing that the growth of hydraulic fractures accounts for 18% to 94% of injection energy. Our results indicate that a large fraction of injected fluid is not stored within the induced fractures. Our results constrain the pore structure response in mudstones to fluid injection and partitioning of fluid between the mudstone matrix and fracture. While more experiments are warranted to draw conclusions, our results can be applied to constrain injection volumes during anthropogenic fluid injection from wastewater disposal, hydraulic fracturing and carbon sequestration.